


 Cite this: *RSC Adv.*, 2019, **9**, 15763

Improving the structural stability and electrochemical performance of $\text{Na}_2\text{Li}_2\text{Ti}_6\text{O}_{14}$ nanoparticles via MgF_2 coating†

 Wei-Wei Ma,^a Hai-Tao Yu,^a Chen-Feng Guo,^a Ying Xie,^a Ning Ren^{*a} and Ting-Feng Yi^a

To improve their electrochemical performance and structural stability, $\text{Na}_2\text{Li}_2\text{Ti}_6\text{O}_{14}$ (NLTO) nanoparticles were synthesized and then coated with a very thin MgF_2 layer. Microscopy confirmed that the MgF_2 -NLTO particles are about 150–250 nm in size, and that the thickness of the MgF_2 layer for the MgF_2 -NLTO-5 sample is ~5 nm. Electrochemical measurements showed that the charge–discharge specific capacities of the five samples under a current density of 50 mA g^{−1} after 100 cycles are 110.4/110.7, 150.7/151.3, 181.1/182.1, 205.7/206.9 and 238.9/239.2 mA h g^{−1}, showing that the performance of MgF_2 -NLTO-5 is the best among all the samples. Thanks to the thin coating layer, the polarization of the anode was reduced significantly, and its reversibility and lithium diffusion dynamics were also improved obviously. The performance improvement can be attributed to the suppression of surface corrosion and the enhancement of structural stability.

Received 30th March 2019

Accepted 4th May 2019

DOI: 10.1039/c9ra02392e

rsc.li/rsc-advances

1. Introduction

Lithium-ion batteries (LIBs) are ubiquitous in our daily lives and serve not only as a means of large-scale energy storage, but also in consumer electronics.¹ In recent years, the increasing demand for safe and high power LIBs has stimulated great research interests in advanced electrode materials.^{2–5} $\text{Na}_2\text{Li}_2\text{Ti}_6\text{O}_{14}$, which has a lower charge–discharge voltage platform (~1.25 V) than $\text{Li}_4\text{Ti}_5\text{O}_{12}$ (1.55 V), is a potential anode material for lithium-ion batteries, and it also exhibits a better ion conductivity and a higher theoretical capacity.⁶ Therefore, a whole battery composed of this material is expected to have a higher output voltage and a higher multiplying capacity, which will be beneficial for applications in the field of electric vehicles.

Although $\text{Na}_2\text{Li}_2\text{Ti}_6\text{O}_{14}$ has many advantages, it still suffers from poor electronic conductivity and sluggish dynamics, which can be solved effectively by nanocrystallization. Aside from the above structural issues, another approach to improve the electrochemical performance of the electrode is to modify the surface status of the materials with inert compounds, to

protect against corrosion from the electrolyte. According to previous studies, metal oxides and metal phosphates are commonly used as coating layers.^{7–15} Nevertheless, it has also been reported that metal oxides and metal phosphates can be converted into corresponding metal fluorides due to the exposure of their surfaces to trace HF in the electrolyte.^{12–14} For instance, Myung *et al.* reported that a metal oxide coating layer on $\text{Li}_{1.05}\text{Ni}_{0.4}\text{Co}_{0.15}\text{Mn}_{0.4}\text{O}_2$ can act as an HF scavenger through the following reaction: $\text{Al}_2\text{O}_3 + 6\text{HF} \rightarrow 2\text{AlF}_3 + 3\text{H}_2\text{O}$.^{16,17} Bai *et al.* reported that the conversion of YPO_4 to YF_3 happens in a $\text{YPO}_4@\text{LiCoO}_2$ system.¹² Moreover, Liu *et al.* indicated that AlF_3 is one of the components of the SEI film formed on the surface of LiCoO_2 immersed in an electrolyte containing an Al_2O_3 additive.¹⁴

Enlightened by previous studies, it can be noted that metal fluorides are most likely the ultimate products on the material surfaces which make a substantial contribution to repeated electrochemical cycling. MgF_2 with high hardness and good thermal stability is widely applied in various optical films and multilayer photonic crystals.¹⁸ Cho *et al.* successfully coated MgF_2 on a LiCoO_2 surface, which improves the electrochemical performance of the material.¹⁹ Moreover, coating MgF_2 on the surface of LiCoO_2 and $\text{Li}[\text{Li}_{0.2}\text{Ni}_{0.2}\text{Mn}_{0.6}]\text{O}_2$ also effectively suppressed their capacity fading.²⁰

To suppress corrosion and improve conductivity simultaneously, coating the nanoparticles with an ultrathin and stable layer offers an effective strategy to significantly improve the electrochemical performance of $\text{Na}_2\text{Li}_2\text{Ti}_6\text{O}_{14}$. Furthermore, for titanium oxide-based anode materials, their electrochemical performance is usually evaluated in the potential window of 1.0

^aKey Laboratory of Functional Inorganic Material Chemistry, Ministry of Education, School of Chemistry and Materials Science, Heilongjiang University, Harbin, 150080, PR China. E-mail: xyieying@hlju.edu.cn

^bZhejiang Chilwee Chuangyuan Industry Co., Ltd, Changxing, Zhejiang 313100, PR China. E-mail: rnrn040412@163.com

^cSchool of Resources and Materials, Northeastern University at Qinhuangdao, Qinhuangdao, 066004, PR China. E-mail: tfyihit@163.com

† Electronic supplementary information (ESI) available. See DOI: [10.1039/c9ra02392e](https://doi.org/10.1039/c9ra02392e)



to 3.0 V vs. Li/Li⁺ to prohibit the formation of an SEI. However, investigations concerning the low potential performance of Na₂Li₂Ti₆O₁₄ are also very important, because they are not only related to energy density but also to safety issues, which are important factors for realistic applications. Our study shows that the coating strategy is workable and that the coated material is very stable and exhibits an excellent electrochemical performance, even discharging down to 0 V. The present study will provide an example for further applications of relevant materials.

2. Experimental section

2.1. Preparation of the samples

The preparation procedure for pure NLTO and MgF₂-coated Na₂Li₂Ti₆O₁₄ is shown in Fig. 1. First, 7.5 mmol titanium sulfate (TiOSO₄) and 7.5 mmol ammonium fluoride (NH₄F) were mixed with 50 mL of ethanol and 25 mL of distilled water under vigorous stirring. The mixture was placed into a Teflon-lined stainless steel autoclave, and a hydrothermal reaction was carried out at 180 °C for 12 h. After the reaction, the product was collected by centrifugation and then washed 3–4 times with distilled water to remove ionic impurities. Finally, the precursors were dried at 60 °C in air. A solid-state reaction was then applied. The precursors, CH₃COOLi·2H₂O, and CH₃COONa, in a molar ratio of 3 : 1 : 1, were pretreated by planetary high energy ball milling in ethanol for 1.5 h and dried in an oven at 60 °C for 6 h. The as-obtained powder was ground and placed in an alumina boat and calcined at 700 °C for 6 h in an air atmosphere to obtain Na₂Li₂Ti₆O₁₄ nanoparticles.

To prepare MgF₂-coated Na₂Li₂Ti₆O₁₄ samples, ammonium fluoride (Aldrich) and magnesium nitrate nonahydrate (Aldrich) were separately dissolved in distilled water. After that, Na₂Li₂Ti₆O₁₄ powder was added to the solution. The Mg : F molar ratio was adjusted to 1 : 2 and the total amounts of MgF₂ in the solution were 0 wt%, 1 wt%, 3 wt%, 5 wt%, and 7 wt%. The

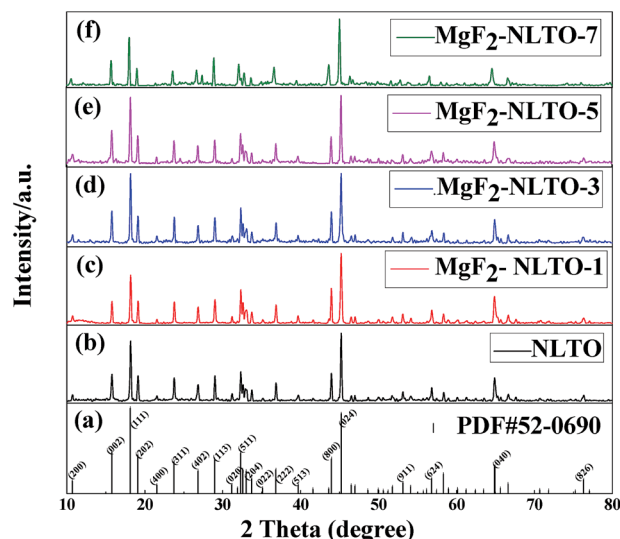


Fig. 2 (a) Standard card for NLTO crystal and XRD patterns for (b) NLTO, (c) MgF₂-NLTO-1, (d) MgF₂-NLTO-3, (e) MgF₂-NLTO-5 and (f) MgF₂-NLTO-7 samples.

solutions were constantly stirred at 80 °C for 5 h, and the obtained powders were heated at 400 °C for 5 h in nitrogen. For convenience, the samples with different amount of MgF₂ were named as NLTO, MgF₂-NLTO-1, MgF₂-NLTO-3, MgF₂-NLTO-5 and MgF₂-NLTO-7.

2.2. Characterization and performance tests

The crystal structure of the samples was studied using a Bruker D8 powder X-ray diffractometer (XRD) and the morphology of the samples was recorded using a scanning electron microscope (SEM, Hitachi S-4800) and a transmission electron microscope (TEM, JEOL2100). Elemental compositions of the sample were characterized *via* energy dispersive spectroscopy (EDS, Oxford INCA Britain). Electrochemical

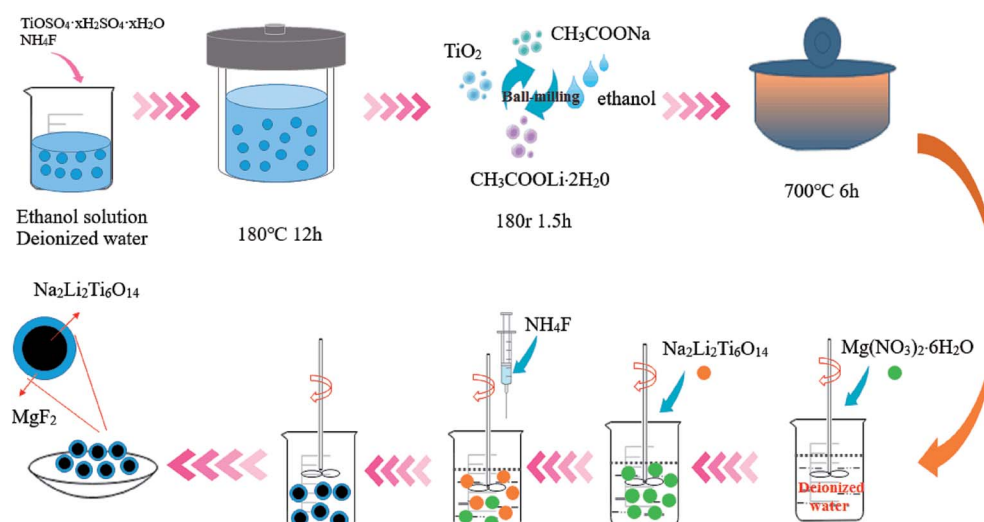


Fig. 1 Schematic diagram for the preparation of NLTO and MgF₂-coated NLTO samples.



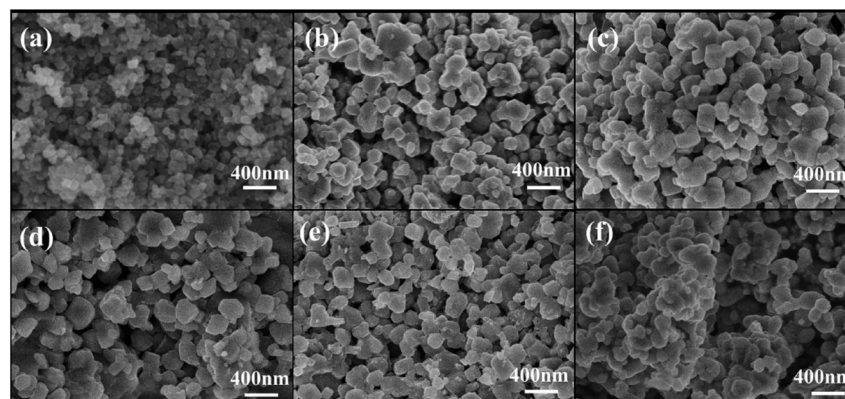


Fig. 3 SEM images of (a) TiO_2 precursor and (b) pure NLTO, and of NLTO powders coated with different amounts of MgF_2 : (c) MgF_2 -NLTO-1, (d) MgF_2 -NLTO-3, (e) MgF_2 -NLTO-5 and (f) MgF_2 -NLTO-7.

tests were performed using CR 2025-type coin cells with pure Li foils as counter electrodes. A mixture of the active material, carbon black, and polyvinylidene fluoride (PVDF) with a weight ratio of 8 : 1 : 1 was homogeneously dissolved in *N*-methyl-2-pyrrolidinone (NMP). The slurry was then pasted on a Cu foil current collector, followed by a vacuum drying process at 110 °C for 12 h. The dried foil was then cut into circular wafers 14 mm in diameter, which were used as cathodes to assemble the half cells in an argon-filled glove box. The oxygen and moisture levels in the glove box were both below 0.1 ppm. The electrolyte was a 1 mol L^{-1} LiPF_6 solution dissolved in a 1 : 1 : 1 (v/v/v) mixture of ethylene carbonate (EC), diethyl carbonate (DEC) and dimethyl carbonate (DMC). Celgard 2400 films were used as separators. Galvanostatic charge-discharge performance was examined using a LAND CT2001A system between 0 and 3 V (vs. Li^+/Li) at different rates. Electrochemical impedance spectroscopy (EIS) tests were performed using a Princeton P4000 workstation over a frequency range from 0.01 Hz to 100 kHz at a potentiostatic signal amplitude of 5 mV. Cyclic voltammetry (CV) tests were carried out using a CHI 1000C electrochemical workstation within a voltage window between 0 and 3 V at a scanning rate of 0.1 mV s^{-1} .

3. Results and discussion

Fig. 2 shows the XRD patterns of pristine and MgF_2 -coated $\text{Na}_2\text{Li}_2\text{Ti}_6\text{O}_{14}$ powders. It was confirmed that the diffraction peaks of NLTO are identical to those of the standard card for $\text{Na}_2\text{Li}_2\text{Ti}_6\text{O}_{14}$ (PDF #52-0690), indicating that NLTO is well crystalline and without impurities. For all MgF_2 -coated samples, the characteristic peaks are almost identical, and the coating of MgF_2 does not significantly affect the lattice structure of NLTO. Fig. S1† displays the Rietveld refinements of all samples. It can be seen that the simulated peaks well match the experimental ones. The refined lattice parameters and errors are listed in Table S1.† The cell parameters of NLTO are calculated to be $a = 5.7370 \text{ \AA}$, $b = 11.2266 \text{ \AA}$ and $c = 16.4844 \text{ \AA}$, and the error (R_{wp}) is only 5.6%.²¹ Compared with NLTO, the cell

parameters of the MgF_2 -coated samples are similar, which further proves that the basic structures of MgF_2 -NLTO remain unchanged after surface modification.

The morphologies of NLTO and MgF_2 -NLTO samples are displayed in Fig. 3. It can be observed that NLTO nanoparticles with sizes of 150–250 nm aggregate together severely. With a coating of MgF_2 , the samples became dispersed uniformly, and their size remains almost the same. These results suggest that the MgF_2 coating layer is thin and beneficial for the dispersion of the sample. Because of the good dispersion and the small size, stacking of the materials would lead to a relative large void space among particles, which is helpful for the penetration of the electrolyte and for the accommodation of lithium. It can thus be anticipated that

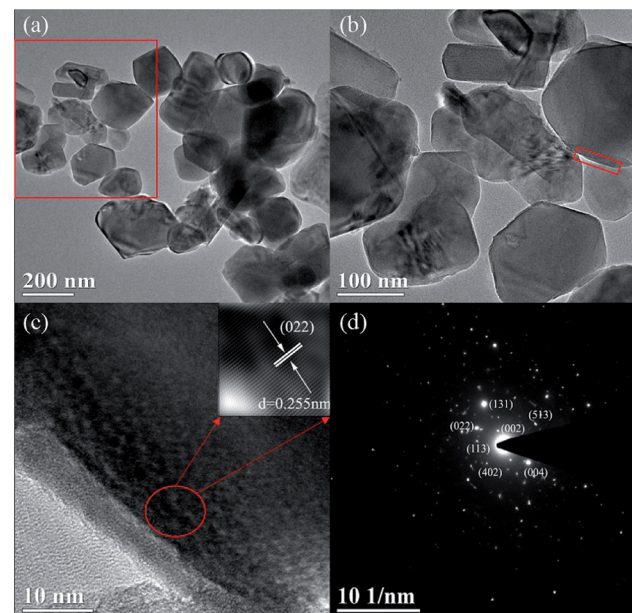


Fig. 4 TEM images for (a and b) the MgF_2 -NLTO-5 sample at different scales, (c) high resolution TEM and relevant lattice fringe in selected area, and (d) SAED pattern.



coating with MgF_2 will improve the electrochemical performance of the materials.

To directly observe the microstructure of the MgF_2 coating layer, TEM images were recorded and compared. Fig. 4 shows the TEM images of the MgF_2 -NLTO-5 sample, and the figure clearly shows that the particle size is around 150–250 nm, which is consistent with the SEM results. Furthermore, the lattice fringe near the crystal surface is about 2.55 Å, which corresponds to the interplanar distance of the (022) facet of NLTO,²² while the light spots in the selection area correlate to the (022), (002), (004), (402) and (113) facets of NLTO. In addition, an amorphous layer with a thickness of ~5 nm can be clearly seen for the MgF_2 -NLTO-5 sample. This coating layer will separate the NLTO from the electrolyte, avoiding direct contact between them two. Thereby, side reactions could be suppressed and the materials should have better stability against HF corrosion. To provide a composition analysis, elemental mapping testing was performed and the results displayed in Fig. 5. The results demonstrate that sodium, titanium, oxygen, fluorine, and magnesium elements are distributed evenly in the whole region of the nanoparticles, and that the MgF_2 layer was coated successfully on the surface of NLTO. These structural changes will be helpful for the enhancement of electrochemical performance.

The CV curves of different samples are shown in Fig. 6. Each curve for different cycles only contains a pair of redox peaks, which corresponds to the insertion/extraction of lithium ions into/from the host structure. For NLTO, the redox peaks appear at 1.43 and 1.21 V in the first cycle, which shifts to 1.42 and 1.17 V and then to 1.44 and 1.15 V in the subsequent two cycles. The redox peaks are the signature of the oxidation of Ti^{3+} and the reduction of Ti^{4+} .^{23,24} To evaluate the polarization, the potential differences between the oxidation and reduction peaks were calculated and are listed in Table S2.† The results indicate that the polarization of NLTO sample increases persistently in the first three cycles, while that of MgF_2 -NLTO-5 is nearly unchanged. At the same time, the peak current for MgF_2 -NLTO-5 remains almost the

same (~0.08 mA) during cycling. The results suggest that the MgF_2 -NLTO-5 sample is quite stable and possesses the lowest polarization. The highly reversible characteristics and the improved electrochemical performance is ascribed to the enhanced structural stability of NLTO caused by the MgF_2 coating.

Fig. 7b–f show the charge–discharge curves of different samples. The charge/discharge capacities of NLTO, MgF_2 -NLTO-1, MgF_2 -NLTO-3, MgF_2 -NLTO-5, and MgF_2 -NLTO-7 in the first cycle were 176.1/292.3, 229.7/384, 216.9/333.4, 267.9/483.4 and 182.3/421.6 mA h g^{−1}, respectively, and their coulombic efficiencies were 60.2%, 59.8%, 65.1%, 55.4% and 43.2%, respectively. The low coulombic efficiencies for the first cycles can be attributed to the formation of a solid electrolyte interface (SEI), the adsorption of lithium ions in the additive, and the irreversible decomposition of the electrolyte.^{25–28} After 10 cycles, their specific capacities became stable and stayed at 149.2, 200.2, 196.3, 231.4 and 160.5 mA h g^{−1}. After 50 cycles, the five samples still possessed high reversible specific capacities of about 120, 160.1, 180.7, 206.4 and 147 mA h g^{−1}. The cyclic performance and coulombic efficiency of the different samples is displayed in Fig. 7a. It can be seen that the specific capacity of NLTO was 110.7 mA h g^{−1} after 100 cycles. With an increasing MgF_2 coating amount, the specific capacity of the samples increases obviously at first and then decreases when the mass ratio of MgF_2 exceeds 7%. This result demonstrates that the introduction of MgF_2 as a protection layer will suppress side reactions at the electrode–electrolyte interface and increase the stability of the material. However, an excessive amount of MgF_2 coated onto the NLTO surface would hinder the exchange of lithium inbetween the electrolyte and NLTO, also leading to poor electrochemical performance. As a result, MgF_2 -NLTO-5 has the best performance, and its specific capacity after 100 cycles is 206.9 mA h g^{−1}.

The rate performances of the samples and the corresponding charge–discharge curves are depicted in Fig. 8. It can be seen from the figure that there is an obvious voltage

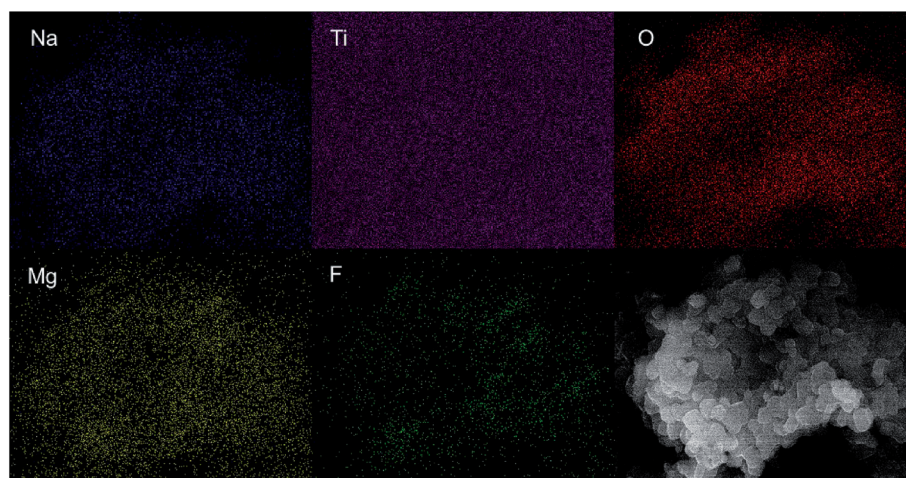


Fig. 5 Elemental mapping for Na, Ti, O, Mg, and F species in the MgF_2 -NLTO-5 sample.



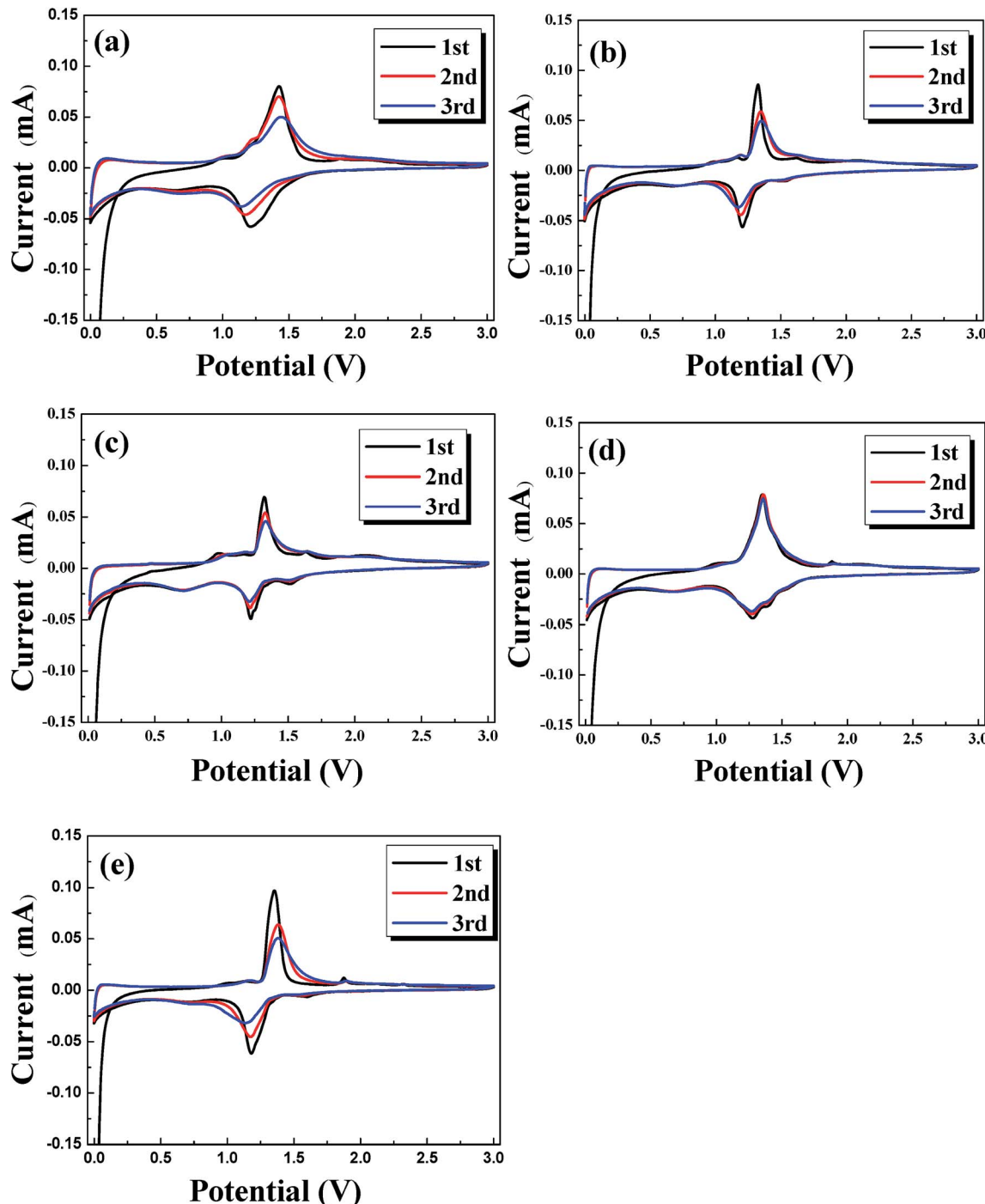


Fig. 6 Cyclic voltammograms (CVs) for the (a) NLTO, (b) MgF_2 -NLTO-1, (c) MgF_2 -NLTO-3, (d) MgF_2 -NLTO-5 and (e) MgF_2 -NLTO-7 samples.

platform at about 1.25 V, which is typical electrochemical behavior of NLTO. The MgF_2 -NLTO samples also show this characteristic platform, indicating that the MgF_2 coating does not change the intrinsic structure of NLTO during cycling. Furthermore, it can be identified that the discharge capacity of the pure NLTO decreases sharply with increasing current density. However, MgF_2 -NLTO samples exhibit much improved performance. In particular, the charge and

discharge capacities of MgF_2 -NLTO-5 (Fig. 8e) both approach 120 mA h g^{-1} at a current density of 2800 mA g^{-1} . Because of the MgF_2 coating, the specific capacities of the MgF_2 -NLTO samples at each rate (Fig. 8a) increase to different extents, and the performance of MgF_2 -NLTO-5 is the best among all the samples. Oppositely, continuously increasing the MgF_2 coating amount results in capacity degradation. This result demonstrates that a suitable coating amount of MgF_2 is

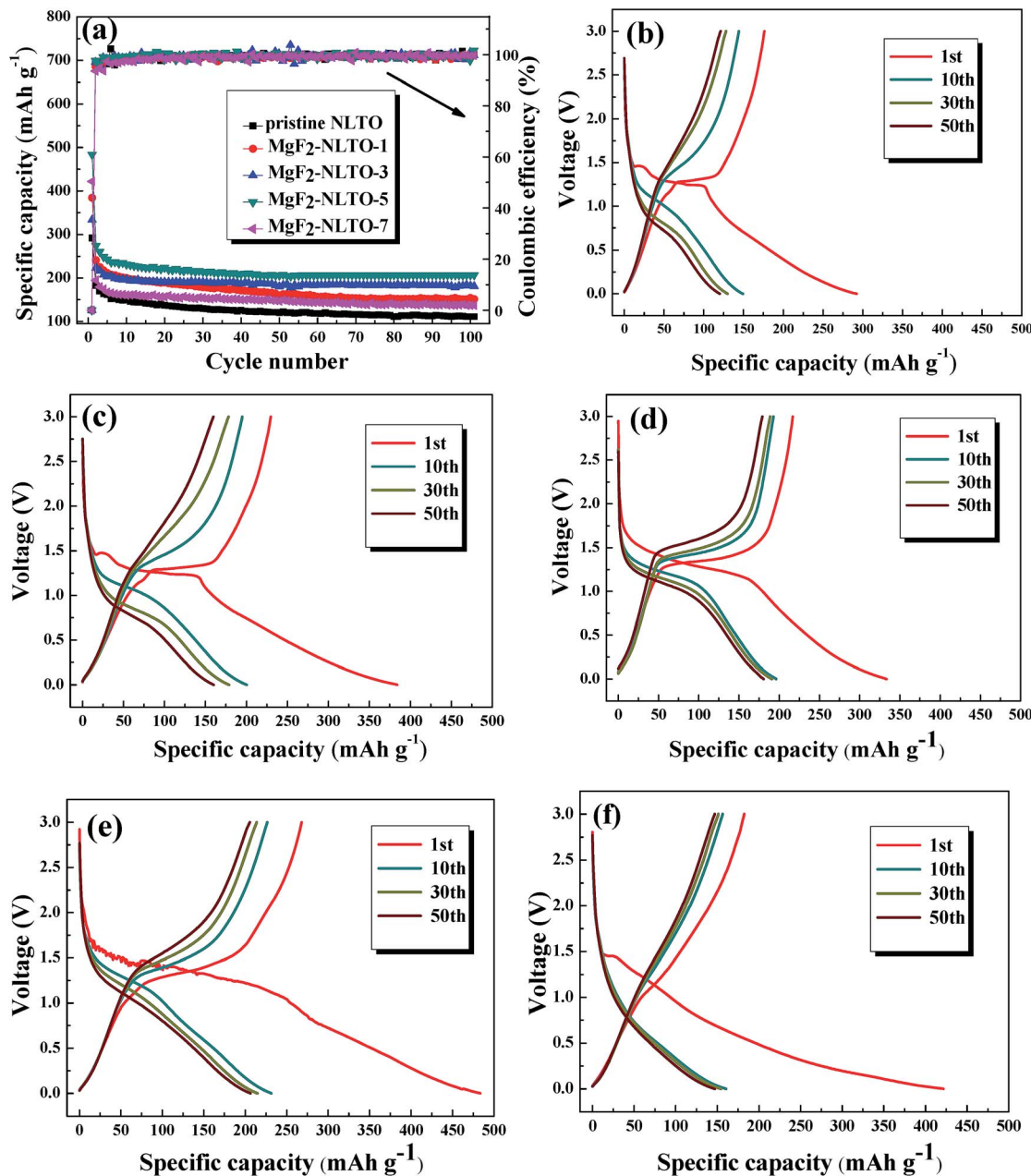


Fig. 7 (a) Cycling performance and coulombic efficiency (at 50 mA g⁻¹) for different samples, and charge-discharge curves for the (b) pure NLTO, (c) MgF₂-NLTO-1, (d) MgF₂-NLTO-3, (e) MgF₂-NLTO-5 and (f) MgF₂-NLTO-7 samples at the 1st, 10th, 30th and 50th cycles.

crucial for optimizing the performance of NLTO, and that a thick MgF₂ coating layer would impede the transport of lithium between NLTO and the electrolyte. In addition, when the current density is reset to 50 mA g⁻¹, the discharge capacity of each sample can be recovered almost to its initial value, which means that the electrochemical reversibility and structural stability of the NLTO host are very good.

To further study the diffusion dynamics of lithium, EIS measurements of the five samples were obtained and the results are displayed in Fig. 9a. The Nyquist curve consists of a concave semicircle in a high frequency region and a straight line in a low frequency region. The former correlates to the

charge transfer resistance (R_{ct}) at the particle-electrolyte interface, while the latter corresponds to the Warburg diffusion process.²² It is found that the R_{ct} of MgF₂-NLTO-5 is much smaller than that of the NLTO, MgF₂-NLTO-1, MgF₂-NLTO-3 and MgF₂-NLTO-7 samples, showing that the structure of MgF₂-NLTO-5 is favorable for charge transfer at the electrode-electrolyte interface.²⁹

Based on Fig. 9a, the diffusion coefficient of lithium ions (D_{Li}) can also be calculated by,³⁰⁻³²

$$Z_{re} = R_{ct} + R_s + \sigma \omega^{-\frac{1}{2}} \quad (1)$$

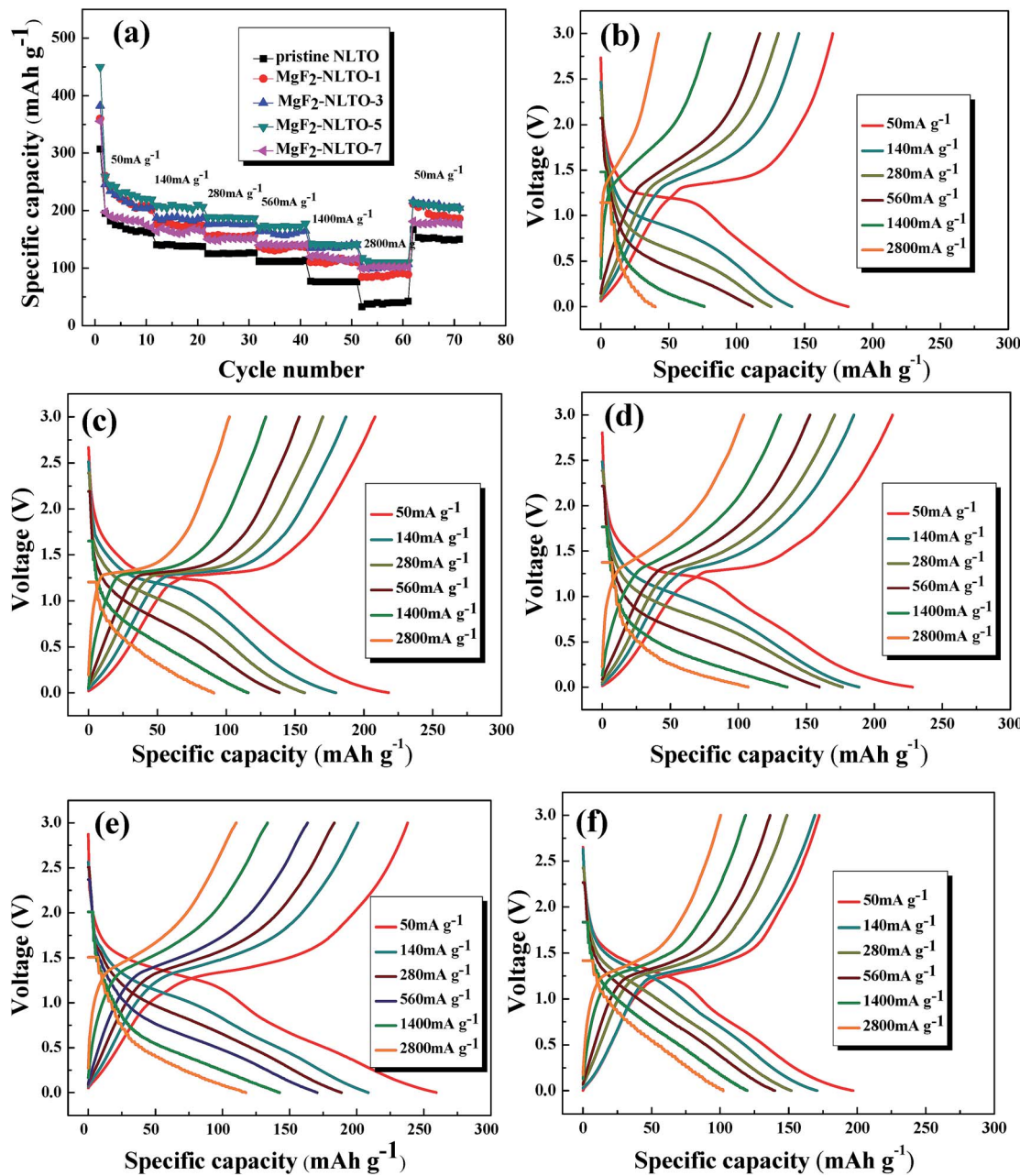


Fig. 8 (a) Rate capabilities for different samples, and charge–discharge curves for the (b) pure NLTO, (c) MgF₂-NLTO-1, (d) MgF₂-NLTO-3, (e) MgF₂-NLTO-5 and (f) MgF₂-NLTO-7 samples under different current densities.

$$D_{\text{Li}} = \frac{R^2 T^2}{2A^2 n^4 F^4 C_{\text{Li}} \sigma^2} \quad (2)$$

where R , T , A , n , F and C_{Li} are the gas constant, the absolute temperature, the surface area of the positive-electrode, the number of electrons transferred in the half-reaction for the redox couple, the Faraday constant, and the concentration of lithium ions in the solid, respectively, while σ denotes the Warburg factor. As reported previously, the relationship between the real part of impedance (Z_{re}) and σ_w is governed by eqn (1).^{33,34} Z_{re} dependence of $\omega^{-0.5}$ is displayed in Fig. 9b. Our calculations indicate that the impedance of NLTO is much

higher than that of the MgF₂-NLTO samples, and that the charge transfer resistance of the MgF₂-NLTO-5 sample is the smallest among all the samples. This result again suggests that the MgF₂ layer has the ability to maintain the surface stability of NLTO and to suppress corrosion by HF, which exists in the electrolyte. According to the above equations, D_{Li} was calculated for all samples, and the values are summarized in Table S3.† MgF₂-NLTO-5 has the highest diffusion coefficient ($2.49 \times 10^{-16} \text{ cm}^2 \text{ s}^{-1}$), implying that the very thin protecting layer is also helpful for improving the diffusion dynamics of lithium.

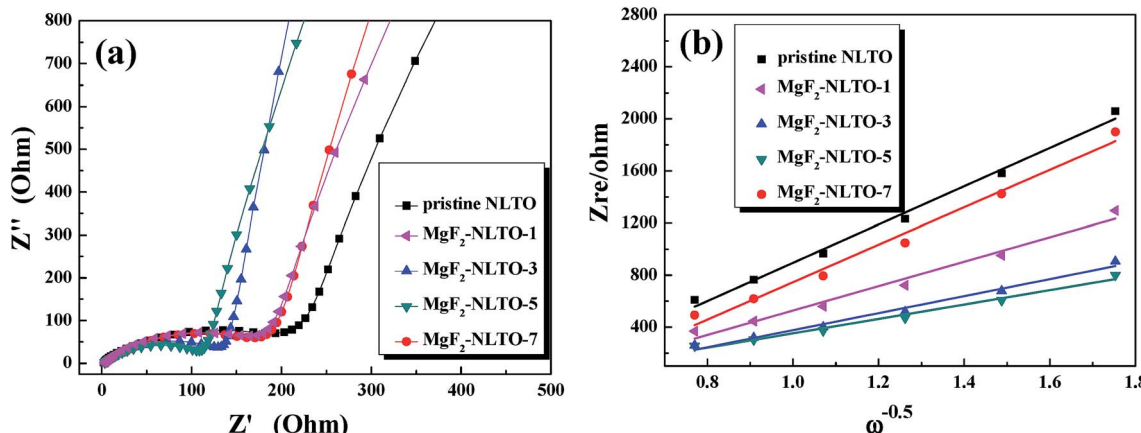


Fig. 9 (a) EIS patterns in a frequency range of 10^{-5} to 10^{-2} Hz with an amplitude of 5 mV and (b) Z_{re} dependence of $\omega^{-0.5}$ in the low frequency region for different samples.

4. Conclusions

MgF_2 was successfully coated on the surface of NLTO nanoparticles *via* a simple chemical deposition method. Experimental results show that MgF_2 -NLTO-5 exhibits the optimal electrochemical performance. Homogeneous coating of MgF_2 on NLTO surface is favorable for the dispersion of the nanoparticles, and it also improves the structural stability of NLTO against corrosion by the electrolyte. As a result, the specific capacity, rate capability, and long-term cycling stability are all improved obviously. Our experiments demonstrate that the combination of nanocrystallization and surface coating techniques is an effective strategy to improve the electrochemical performance of NLTO, which may be helpful for the design and optimization of relevant electrode materials.

Conflicts of interest

There are no conflicts to declare.

Acknowledgements

This work was financially supported by the National Natural Science Foundation of China (No. 21773060 and 51774002), Fundamental Research Funds for the Central Universities (No. N182304014), Natural Science Foundation of Heilongjiang Province (E2016056), Fundamental Research Funds for Heilongjiang University of Heilongjiang Province (HDRCCX-2016Z03), Youth Innovation Team Project of Science and Technology of Heilongjiang University (RCYJTD201803), and Young Scholar Project of the Long Jiang Scholars Program (Q201818).

References

- 1 J. Lee, A. Urban, X. Li, D. Su, G. Hautier and G. Ceder, *Science*, 2014, **343**, 519–522.
- 2 X. F. Zhang, I. Belharouak, L. Li, Y. Lei, J. W. Elam, A. Nie, X. Q. Chen, R. S. Yassar and R. L. Axelbaum, *Adv. Energy Mater.*, 2013, **3**, 1299–1307.
- 3 B. Dunn, H. Kamath and J. M. Tarascon, *Science*, 2011, **334**, 928–935.
- 4 X. L. Wu, Y. G. Guo, J. Su, J.-W. Xiong, Y. L. Zhang and L. J. Wan, *Adv. Energy Mater.*, 2013, **3**, 1155–1160.
- 5 L. Zeng, C. Zheng, C. Deng, X. Ding and M. Wei, *ACS Appl. Mater. Interfaces*, 2013, **5**, 2182–2187.
- 6 D. Dambournet, I. Belharouak and K. Amine, *Inorg. Chem.*, 2010, **49**, 2822–2826.
- 7 Y. Wu and A. Manthiram, *Electrochem. Solid-State Lett.*, 2006, **9**, 221–224.
- 8 J. Liu, B. Reeja-Jayan and A. Manthiram, *J. Phys. Chem. C*, 2010, **114**, 9528–9533.
- 9 Y. K. Sun, Y. S. Lee, M. Yoshio and K. S. Amine, *Electrochem. Solid-State Lett.*, 2002, **5**, 99–102.
- 10 J. Cho, T. J. Kim, J. Kim, M. Noh and B. Park, *J. Electrochem. Soc.*, 2004, **151**, 1899–1904.
- 11 Y. Bai, Q. Chang, Q. Yu, S. Zhao and K. Jiang, *Electrochim. Acta*, 2013, **112**, 414–421.
- 12 Y. Bai, Y. Yin, N. Liu, B. Guo, H. Shi, J. Liu, Z. Wang and L. Chen, *J. Power Sources*, 2007, **174**, 328–334.
- 13 S. T. Myung, K. Izumi, S. Komaba, Y. K. Sun, H. Yashiro and N. Kumagai, *Chem. Mater.*, 2005, **17**, 3695–3704.
- 14 J. Y. Liu, N. Liu, D. T. Liu, Y. Bai, L. H. Shi, Z. X. Wang, L. Q. Chen, V. Hennige and A. Schuch, *J. Electrochem. Soc.*, 2007, **154**, 55–63.
- 15 J. M. Zheng, M. Gu, J. Xiao, B. J. Polzin, P. F. Yan, X. L. Chen, C. M. Wang and J. G. Zhang, *Chem. Mater.*, 2014, **26**, 6320–6327.
- 16 S. T. Myung, K. Izumi, S. Komaba, H. Yashiro, H. J. Bang, Y.-K. Sun and N. Kumagai, *J. Phys. Chem. C*, 2007, **111**, 4061–4067.
- 17 Q. L. Xie, Z. B. Hu, C. H. Zhao, S. R. Zhang and K. Y. Liu, *RSC Adv.*, 2015, **5**, 50859–50864.
- 18 Y. Bai, K. Jiang, S. Sun, Q. Wu, X. Lu and N. Wan, *Electrochim. Acta*, 2014, **134**, 347–354.



19 Y. Cho, J. Eom and J. Cho, *J. Electrochem. Soc.*, 2010, **157**, 617–624.

20 H. J. Lee and Y. J. Park, *Solid State Ionics*, 2013, **230**, 86–91.

21 D. Dambournet, K. W. Chapman, M. V. Koudriachova, P. J. Chupas, I. Belharouak and K. Amine, *Inorg. Chem.*, 2011, **50**, 5855–5857.

22 K. Q. Wu, J. Shu, X. T. Lin, L. Y. Shao, P. Li, M. Shui, N. P. Long and D. J. Wang, *J. Power Sources*, 2015, **275**, 419–428.

23 K. Q. Wu, J. Shu, X. T. Lin, L. Y. Shao, P. Li, M. Shui, M. M. Lao, N. P. Long and D. J. Wang, *Electrochim. Acta*, 2015, **173**, 595–606.

24 S. Y. Yin, C. Q. Feng, S. J. Wu, H. L. Liu, B. Q. Ke, K. L. Zhang and D. H. Chen, *J. Alloys Compd.*, 2015, **642**, 1–6.

25 P. F. Wang, P. Li, T. F. Yi, X. T. Lin, H. X. Yu, Y.-R. Zhu, S. S. Qian, M. Shui and J. Shu, *J. Power Sources*, 2015, **297**, 283–294.

26 W. J. H. Borghols, M. Wagemaker, U. Lafont, E. M. Kelder and F. M. Mulder, *J. Am. Chem. Soc.*, 2009, **131**, 17786–17792.

27 T. F. Yi, Y. Xie, J. Shu, Z. H. Wang, C. B. Yue, R. S. Zhu and H. B. Qiao, *J. Electrochem. Soc.*, 2011, **158**, 266–274.

28 T. F. Yi, S. Y. Yang and Y. Xie, *J. Mater. Chem. A*, 2015, **3**, 5750–5777.

29 O. Toprakci, H. A. K. Toprakci, Y. Li, L. W. Ji, L. G. Xue, H. Lee, S. Zhang and X. W. Zhang, *J. Power Sources*, 2013, **241**, 522–528.

30 S. Y. Yang, J. Yuan, Y. R. Zhu, T. F. Yi and Y. Xie, *Ceram. Int.*, 2015, **41**, 7073–7079.

31 M. M. Lao, P. Li, X. T. Lin, L. Y. Shao, M. Shui, N. B. Long, D. J. Wang and J. Shu, *RSC Adv.*, 2015, **5**, 41999–42008.

32 C. J. Jafta, K. I. Ozoemena, M. K. Mathe and W. D. Roos, *Electrochim. Acta*, 2012, **85**, 411–422.

33 Y. S. Hu, L. Kienle, Y. G. Guo and J. Maier, *Adv. Mater.*, 2006, **18**, 1421–1426.

34 T. F. Yi, S. Y. Yang, X. Y. Li, J. H. Yao, Y. R. Zhu and R. S. Zhu, *J. Power Sources*, 2014, **246**, 505–511.

